Heliyon 10 (2024) e24585

Contents lists available at ScienceDirect

Heliyon

journal homepage: www.cell.com/heliyon

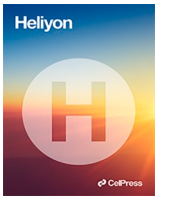

Research article

Polarization manipulation on step-index composite polymer beam splitters for photonics circuitry

Noor Afsary [a], Fariha Tasnim [a], Md Omar Faruk Rasel [a,*], Takaaki Ishigure [b]

[a] Physics Discipline, Khulna University, Khulna, 9208, Bangladesh
[b] Faculty of Science and Technology, Keio University, Yokohama, 223-8522, Japan

ARTICLE INFO

Keywords:
Polarization manipulation
Step-index core
Alternating direction implicit (ADI) method
Composite coupler
Polymer optical waveguides

ABSTRACT

This paper presents composite beam splitters realized with polymer materials for developing photonic integrated circuits. We used organic-inorganic hybrid polymer materials to form this composite beam splitter realized with step-index (SI) core profiles. We used the alternating direction implicit technique of the Rsoft CAD BeamPROP solver to design and analyze these beam splitters. We successfully examined and manipulated the beam splitter's polarization dependency to obtain a 99% output efficiency with a 50:50 splitting ratio. The SI beam splitter exhibits an excess loss of 0.014 dB. When we apply polarized light in this beam splitter, the excess loss increases to 2 dB, and this loss gradually decreases as the angle of incident light increases. The excess loss reduces to 0.05 dB at the 31-degree angles of the incident polarized light. We also investigated the crosstalk of this beam splitter by varying the wavelength, and it is evident that the lowest crosstalk is −19.77 dB at the polarized angle of 31°.

1. Introduction

Since the bandwidth demand for high-performance computing systems (HPCs), supercomputers, and high-end servers is increasing, optical interconnects can be a candidate technology to meet the growing bandwidth demands over electrical interconnects because optical interconnects can transmit signals at the speed of light [1]. Optical interconnects offer several advantages over electrical interconnects, including high-speed data transmission with minimal loss, low energy consumption, and reduced unwanted crosstalk [2,3]. Short-reach optical interconnects, particularly optical waveguides, provide adaptability and reliability owing to their ease of integration into printed circuit boards (PCBs) and photonic integrated circuits (PICs) [4]. Researchers are developing various configurations of optical waveguides to address the increasing bandwidth requirements and achieve high-density wiring on PCBs [5–7]. Polymer waveguides offer numerous benefits for board-level applications, including high-density wiring, cost-effectiveness, flexibility, ease of manufacture, and tolerance to fabrication errors [8,9]. However, polymer waveguides with high-index contrast introduce significant polarization effects, necessitating the use of polarization beam splitters (PBS) [10].

Over the past few years, directional couplers employing a PBS have drawn substantial attention owing to their vast array of applications [11,12]. Researchers have demonstrated an asymmetric directional coupler with incompatible air cladding to achieve vertical symmetry through a PBS, which is vulnerable to manufacturing imperfections [13]. However, employing metamaterials in directional coupler construction presents specific challenges and significant material costs [14,15]. The polymer directional coupler

* Corresponding author.
E-mail address: ofr_ju@phy.ku.ac.bd (M.O.F. Rasel).

https://doi.org/10.1016/j.heliyon.2024.e24585
Received 23 September 2023; Received in revised form 9 January 2024; Accepted 10 January 2024
Available online 17 January 2024

introduced in Ref. [16] demonstrated low excess loss and favorable coupling ratios; further investigation is required to assess its polarization dependence. Directional couplers have applications in optical switches, waveguide interferometers, sensors, and multiplexing devices, offering efficient solutions for short-reach optical interconnects [17–19]. Step-index (SI) polymer waveguides have emerged as the preferred choice for optical communication systems because of their ease of fabrication and compatibility with various materials [20,21]. However, SI-based waveguides exhibit diverse polarization states, necessitating the use of PBS and interferometers to align the light-wave polarization [22,23]. Although slot waveguides can achieve polarization-independent splitting, sourcing suitable materials for fabrication can be challenging. Even when using polymer materials with polarization dependency, manipulating the polarization is highly desirable. Prior research has demonstrated the effectiveness of graded-index PBS with polymer directional couplers, showing excellent beam-splitting capabilities and a high polarization extinction ratio [24].

This paper presents polymer-based composite beam splitters with SI core profiles using the beam propagation method (BPM). We used the alternating direction implicit (ADI) technique to investigate the beam splitter. We demonstrate the output efficiency of these beam splitters with a uniform splitting ratio, coupling ratio, excess loss, and crosstalk with and without the polarization effect.

2. Materials and methods

2.1. Theory

The theory of directional couplers encompasses waveguide interactions, wherein two waveguides are placed near the separation gap along their length, which is denoted as the coupling length. The coupling characteristics of directional couplers can be elucidated using coupled-mode theory [25]. This theory demonstrates the mode coupling coefficients by transferring light between the closely separated waveguides, and the parameter that describes the power transfer phenomena between the waveguides is known as the beat length (L_c) using equation (1) [26] as follows:

$$L_c = \frac{\pi}{\kappa} = \frac{\lambda}{2[n_{even} - n_{odd}]} = \frac{\lambda}{2\Delta n} \tag{1}$$

The symbol κ represents the coupling coefficient, and n_{even} and n_{odd} denote the effective indices of the even and odd symmetric modes, respectively. The ADI method is employed to analyze the characteristics of the 3D directional couplers. Maxwell's equations govern the electromagnetic behavior of the 3D directional couplers. We use a computational mesh to discretize these equations and employ explicit and implicit time-stepping methods to solve these equations. The resulting system is advanced in time using the ADI approach [27]. The process of determining appropriate parameter values for the entire vectorial calculation of a directional coupler, as referenced in Ref. [28], is called scheme parameter selection for the ADI method. The stability of the system depends on the scheme parameters, particularly when dealing with high-index contrast or small grid sizes in the RSoft CAD simulation setup. The precise values of the parameters of the scheme, including the time-step size, mesh size, and boundary conditions, can vary based on the coupler's performance characteristics and structural design requirements. This investigation reveals that a scheme parameter value of 0.5 yields simulation results that exhibit the highest level of precision and reliability for the directional coupler. We achieve this optimal outcome by varying the scheme parameter from 0.5 to 1, as shown in Fig. 1. The scheme parameters determine the relative importance of the explicit and implicit stages of the ADI technique. According to Fig. 1, we choose the scheme parameter 0.5 to investigate the precision and numerical stability of the simulation outcomes.

We characterize the directional couplers by employing the transfer matrix [29,30], denoted as T, which demonstrates the directional couplers in equation (2) as follows:

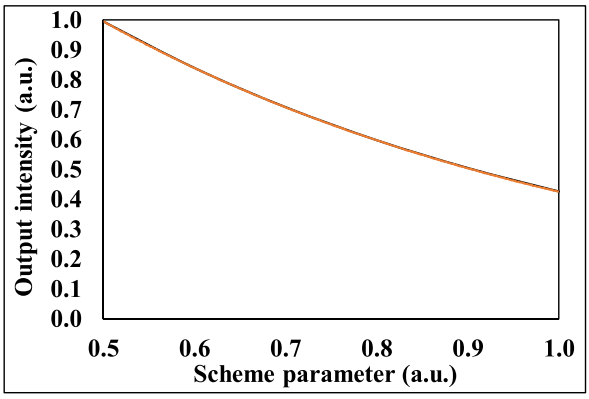

Fig. 1. The scheme parameter varies as a function of the output intensity , which causes inaccuracies and numerical instability when the scheme parameter is lower than 0.5.

$$T = \begin{bmatrix} \frac{\cos(\beta_c L) - j\Delta\beta L \sin(\beta_c L)}{2j\Delta\beta L} \sin(\beta_c L) \\ \hline 2 \end{bmatrix} \cos(\beta_c L) \tag{2}$$

$$= sign\,[\cos\varphi] \begin{pmatrix} cos^2\,\varphi & \cos\varphi \sin\varphi \\ \cos\varphi \sin\varphi & sin^2\,\varphi \end{pmatrix}$$

where β_c is the propagation constant of the coupled mode, Δβ is the phase constant difference between the two waveguides, L is the coupling length, and $\boldsymbol{\varphi}$ is the angle of the Jones matrix at which the light is launched at the input. We utilize the transfer matrix to calculate the directional coupler output fields by considering the input parameters and coupling coefficients. In the BPM simulations, we represent the directional coupler as a 3D waveguide structure, considering the full-vectorial form of the electromagnetic field. The BPM algorithm numerically solves Maxwell's equations using the ADI method to propagate the electromagnetic field within waveguides. This algorithm calculates the intensity distribution and phase of the electric field at each iteration by using the waveguide properties and coupling coefficients between the waveguides.

2.2. Design and optimization

The schematic details of the composite beam splitter (CBS) are illustrated in Fig. 2. The structural presentation of this beam splitter is as follows: Two straight waveguides are connected to another two S-bend waveguides, and the output of these S-bends is connected to another two straight waveguides in the central region, known as the coupling region. The outputs of the coupling waveguides are then connected to two other S-bend waveguides, followed by two output waveguides. To fabricate the CBS, we used SUNCONNECT, an organic-inorganic hybrid resin provided by Nissan Chemical Corporation Ltd., Japan. The core and cladding materials are NP-005 ($n_1 = 1.575$) and NP-211 ($n_2 = 1.567$) at 1550 nm. These materials demonstrate minimal absorption loss, which is attributed to the lower density of the carbon-hydrogen bonds within the resins. The polymer-based CBS schematics, shown in Fig. 2, can be fabricated using the imprint technique explained in Refs. [31,32]. The details of the imprint fabrication technique are as follows: First, the cladding monomer is placed inside the silicone frame on the glass substrate. Grooves for the square-shaped cores are formed on the under-cladding by pressing a stamp mold with a negative photo-resist made of polydimethyl-siloxane, and the mold-based under--cladding is cured using UV exposure. To fabricate a single-mode waveguide, the dimensions of the mold patterns should satisfy the single-mode condition. Next, the polydimethyl-siloxane mold is peeled off and the grooves are filled with the liquid core monomer, followed by UV exposure. Finally, cladding monomer is placed on the core layers to form the upper cladding layer. The waveguide is then cured by UV exposure followed by a post-backing process.

The core width should be less than 7 μm to maintain the single-mode condition at 1550 nm. Therefore, we set the core width to 6 μm and the cross-sectional dimensions to 6 × 6 μm^2. This device exhibits a typical SI-type square core. In our simulation solver, we incorporated this index profile using the power-law approximation equations (3) and (4) [33], as follows:

$$n(r) = n_1 \sqrt{1 - 2\Delta \left(\frac{r}{a}\right)^g} \tag{3}$$

$$\Delta = \frac{n_1^2 - n_2^2}{2n_1^2} \tag{4}$$

here, variables a and g represent the radius and exponential coefficient, respectively. Also, n_1 and n_2 are the refractive indices of the core and cladding materials, respectively. Coefficient g is as an indicator of the shape of the index profile. We set the value of g to be large (more than 2) to form an SI waveguide. Fig. 3(a) presents the index profile of the SI CBS with a uniform intensity distribution (indicated by the red color) throughout the core. Fig. 3(b) shows the refractive-index profile, where the index is almost uniformly distributed across the cores.

We optimize the polymer-based CBS by investigating the following parameters: the S-bend waveguide, the separation gap between the two straight input waveguides, and coupling-region waveguides. First, we investigate the S-bend waveguides by varying the

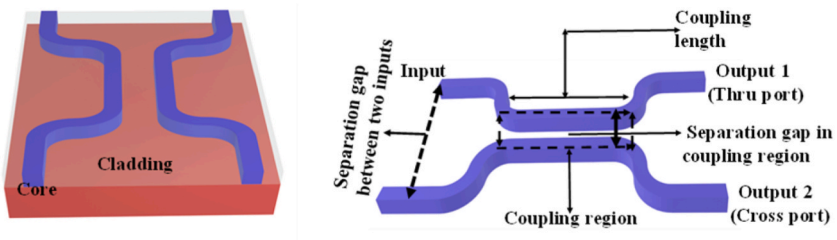

Fig. 2. Schematic details of the symmetric composite beam splitter. (a) Top view. (b) Parameter details in the CBS.

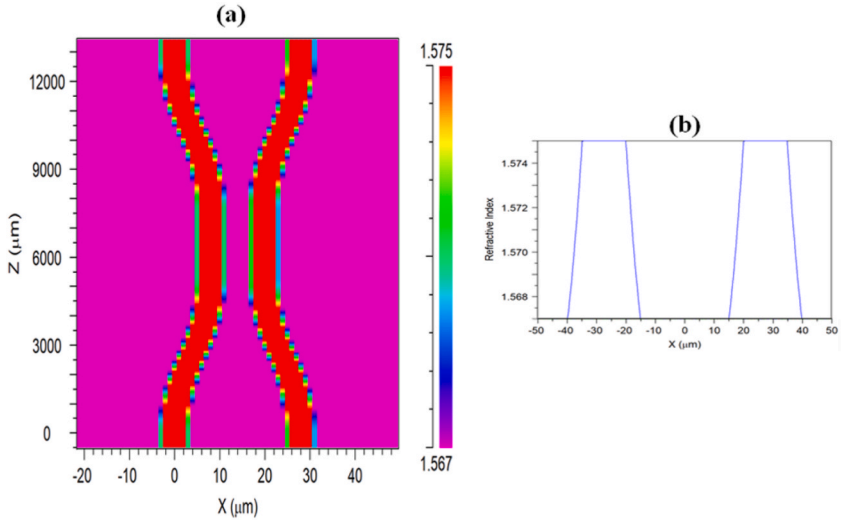

Fig. 3. (a) A uniform index distribution through the SI beam splitter. (b) index profiles.

bending radius (which automatically changes with the bending length), and the output intensity is shown in Fig. 4. Here, we confirm that the optimal length of the S-bend structure is 5311 μm, which corresponds to the maximum output intensity. We simultaneously examine the separation gap between the two inputs and coupling length to determine the mode-coupling distance of the beam splitter, as shown in Fig. 5(a) and (b). Fig. 5(a) shows the optimization of the separation gap between the two inputs as a function of the coupling length for the thru port, and Fig. 5(b) shows the optimization through the cross port. The color bars on the right in Fig. 5(a) and (b) indicate the intensities observed in the ports. These figures show that the cross-port demonstrates minimal intensity, whereas the thru-port shows maximum intensity, except for the region represented by the dotted line. The black dotted line region (with a separation gap of 28–30 μm and coupling length of 1000–5000 μm) demonstrates equal intensity (50:50 splitting ratio) between the outputs. The separation gaps between the input and output waveguides should be identical.

We further investigated the separation gap between the input waveguides and coupling length as a function of the output intensity. Fig. 5(c) shows an equal output intensity when the coupling length is 2290 μm, and we set the coupling length to 2290 μm for this CBS. Similarly, Fig. 5(d) shows that the output intensity varies with the separation gap between the inputs, and this beam splitter exhibits a splitting ratio of 49:50 when the separation gap between the inputs is 29 μm. Finally, we investigate the separation gap between the input waveguides and coupling-region waveguides and confirm that the separation gap between the coupling-region waveguides is 7 μm when the separation gap between the input waveguides is 29 μm, as shown in Fig. 5(e). Table 1 lists the optimized parameters of the 3D SI beam splitter.

3. Results and discussion

3.1. Performance analysis

This study investigates the functioning of a polymer SI CBS with a 50:50 splitting ratio. The beam splitter uniformly distributes light between the thru port, supporting the transverse electric (TE) mode and the cross port, maintaining the transverse magnetic (TM)

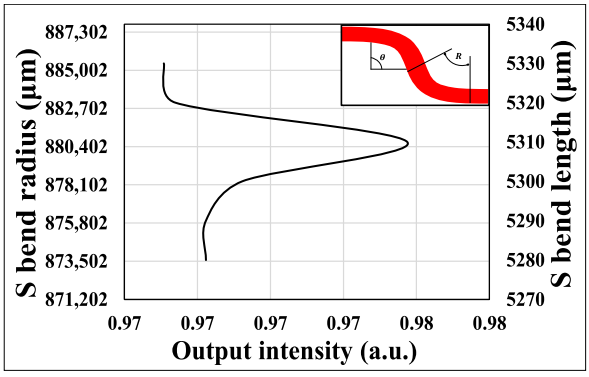

Fig. 4. S-bend waveguide optimization. Here, the bending radius automatically changes with the bending length.

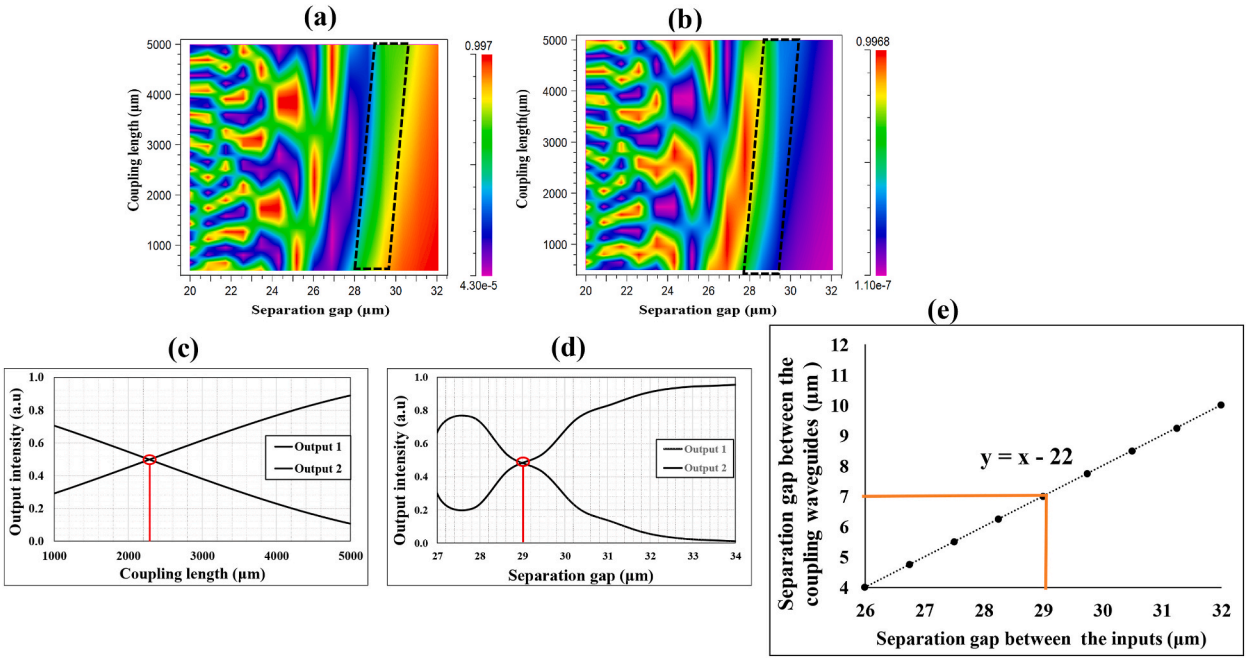

Fig. 5. Optimization of the coupling length as a function of the separation gap at the input waveguides. (a) Thru port optimization. (b) Cross port optimization. (c) Coupling length as a function of output intensity for equal splitting ratio. (d) Separation gap optimization between the two inputs. (e) Separation gap between the inputs as a function of the separation gap between coupling region. Here, $y = x - 22$ represents the relationship between the separation gap between the coupling waveguides and the input waveguides.

Table 1
The parameters governing the performances of the polymer-based SI directional couplers.

Parameters	Values
Input/output waveguide	500 μ m
Diameter of core	6 μ m
The bend waveguide length	5311 μm
Bend waveguide radius of curvature	881,130 μm
Coupling length	2290 μm
The separation gap between the waveguides at the coupling region	7 μm
Separation gap between the two inputs	29 μm

mode, as illustrated in Fig. 6(a). The simulation data precisely quantifies the field intensity between outputs. The intensity values for the TE and TM modes are 0.496 a.u. and 0.500 a.u., respectively, closely matching the 50:50 splitting ratio. Fig. 6(b) illustrates the 3D intensity distribution among both outputs, indicating equal heights at the two output ports. The mode profile for the two output ports is illustrated as near-field patterns in Fig. 6(c), where the waveguide core (highlighted in red) exhibits a symmetric output. We observe an equal distribution of light across both the output ports. In addition, we calculate the intensity propagation through the SI beam splitters, and the results are shown in Fig. 6(d). The findings indicate that light travels through both outputs, achieving an equal splitting ratio of 50:50 with a wavelength variation of 1.53–1.56 μm, as shown in Fig. 6(e). Thus, the beam splitter exhibits an output efficiency of 99%.

3.2. The polarization effect

The polarization effect is examined in this study using the ADI full-vector model with the Jones Matrix [27,30]. This matrix can alter the polarization state of the incident field. We examine the linear polarization phenomenon of the input light in the beam splitter. The TE mode remains the same waveguide and propagates into the thru port (output 1), whereas the TM mode exits via the cross port (output 2), as shown in Fig. 7(a). Fig. 7(b) shows the output intensity resulting from the linear polarization effect. The solid red curves in the figure represent the polarization effect, whereas the black dotted lines indicate no polarization influence. In the absence of polarization, the input power of the beam splitters is approximately 1.0 a.u. However, including the polarization effect causes the input power to decrease to 0.6342 a.u. Therefore, polarization manipulation is employed to achieve a high coupling efficiency at the input in the subsequent section. Polarization manipulation is used to enhance the coupling efficiency of the incident light in the context of a directional coupler. The Jones Matrix introduces linearly polarized light into the input port at specific angles. These angles are chosen

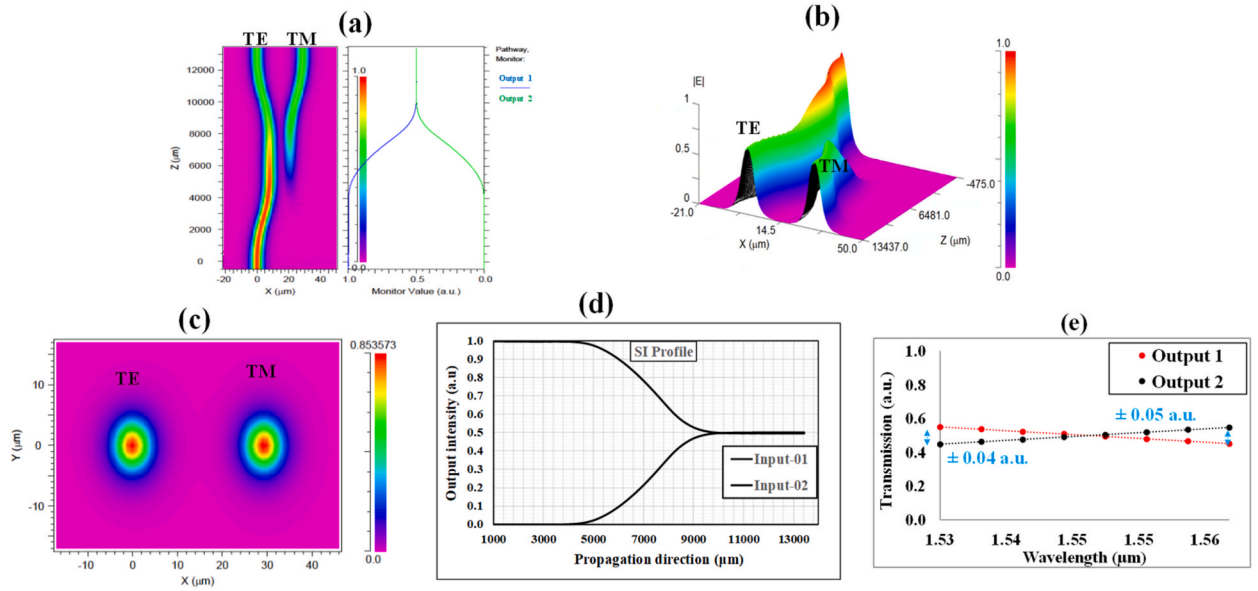

Fig. 6. (a) Optical energy distribution of the composite beam splitter. (b) The 3D intensity distribution of the 50:50 beam splitter. (c) Near-field patterns of the splitters. (d) Normalized intensity distribution via the outputs along the propagation direction. (e) Output splitting depends on the wavelength from 1.53 to 1.56 μm as a transmission function.

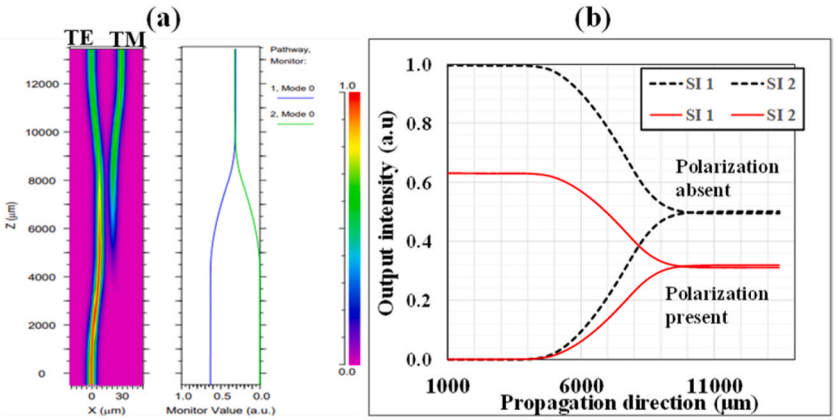

Fig. 7. (a) Effects of applying linear polarization to the splitter (applying linear polarization makes the input intensity decrease by almost 37%). (b) Intensity distribution before and after using polarization (with a noticeable reduction in intensity when polarization is applied).

to optimize the coupling efficiency between the light and the input waveguides. We increased the angle of the incident light and plotted the results in Fig. 8. Fully polarized light is introduced into the input at various polarized angles, which indicate the orientation of the input light with the polarizer. We varied the polarization angles to 0–35° and determined suitable polarization angles by employing the trial-and-error method. When the incident polarized angle is 0 °, the input intensity reduces to 0.6 arbitrary units (a.u.).

Simultaneously, the output efficiency reaches a minimum value of approximately 56%, as indicated by the red dotted line. The data presented in Fig. 8 demonstrate that the input and output efficiencies of polarized light approach equality and maximum efficiency when the incident angle of light is 31 ° or 32 °. When the incident angle is greater than 32 °, the output intensity is greater than 1 (a.u.), which is impossible in practice. Therefore, at the 31-degree incident angle, the output efficiency improved by nearly 70% compared to that at 0 ° with minimum insertion loss. The blue dotted lines indicate an enhancement of 95% in the efficiency of the SI beam splitters. Hence, we set the polarized incident angle of the SI beam splitter is of 31 °. Therefore, polarization manipulation reduces the input coupling loss and improves the efficiency as the absence of polarization, as shown in Fig. 7(b).

3.3. Variation of numerical aperture

The numerical aperture (NA) characterizes the light-capturing ability of optical devices. The NA of a waveguide depends on the

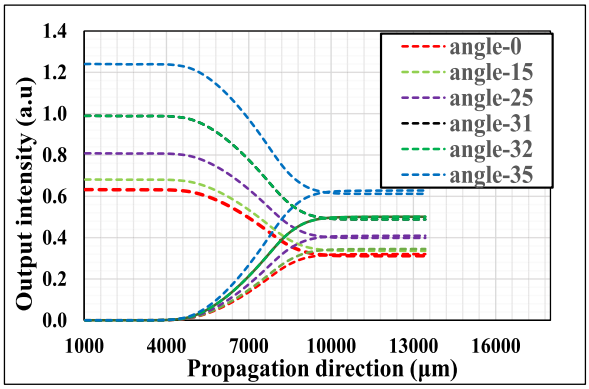

Fig. 8. Output intensity variation with the different polarized angles of the SI beam splitters.

combination of core and cladding materials. We calculated NA by employing the equation provided in equation (5) [34] as follows:

$$\mathrm{NA} = \sqrt{n_1^2 - n_2^2} \tag{5}$$

The theoretical relationship between the numerical aperture and light collection efficiency is often expressed in terms of the light-gathering ability of the system in equation (6).

$$\text{Light Collection Efficiency} \propto NA^2 \tag{6}$$

A higher NA allows the beam splitters to collect light from a wider angular range. The efficiency of the beam splitters depends on the well-matched NA of the materials, which can optimize the efficiency of the beam splitters. We examine the output intensity of the beam splitters by varying the NA, and the output results are shown in Fig. 9. The splitter has no beam-splitting property when the NA is 0.177, as shown by the solid black line. When the NA is 0.158, the splitter exhibits an equal splitting ratio, as indicated by the red dotted lines. In contrast, when the NA decreases to 0.137, the splitters can function as switching devices for both the TE and TM modes.

3.4. Splitting ratio and full width at half maximum

We present a polymer-based beam splitter with a 50:50 splitting ratio at 1550 nm, as illustrated in Fig. 10. From this figure, we find that this beam splitter can act as a TE/TM mode switch, allowing for wavelength flexibility (from 1.30 to 1.70 μm). We investigate the significance of the full width at half maximum (FWHM) of the directional coupler because it can evaluate the spectral response precision of the coupler by quantifying the wavelength range where the coupling ratio is half of its peak value. We assess the FWHM for different phase angles (φ) to understand how the coupler responds to varying polarization conditions, as shown in Fig. 11(a). The phase angle (φ) is obtained from the output field in the polar coordinates of the far-field transformation, as shown in Fig. 11 (b). The far-field intensity of the beam splitter is focused on the distribution of the field intensity at various angles in the far-field region. A wider FWHM signifies a less precise coupling over a broader spectrum, potentially affecting the integrity of the output signal. In particular, a narrower FWHM indicates greater focus on coupling. We varied the wavelength from 1300 to 1700 nm and plotted the FWHM with phase angles of 0 ° and 90 ° in Fig. 11(a). At 1550 nm, our proposed splitter exhibits a minimal FWHM of 4.67 and 7.74° for φ = 0 and φ = 90°, respectively, indicating precise coupling.

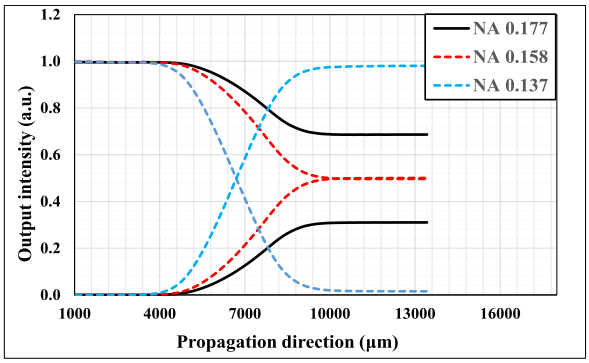

Fig. 9. Output intensity due to the numerical aperture variation along the propagation direction of the PBS.

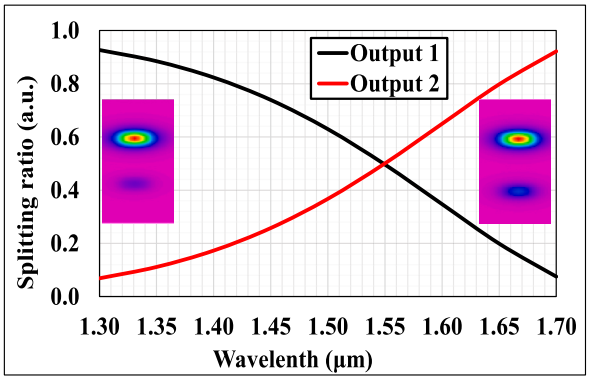

Fig. 10. The splitting ratio versus wavelength for the coupler.

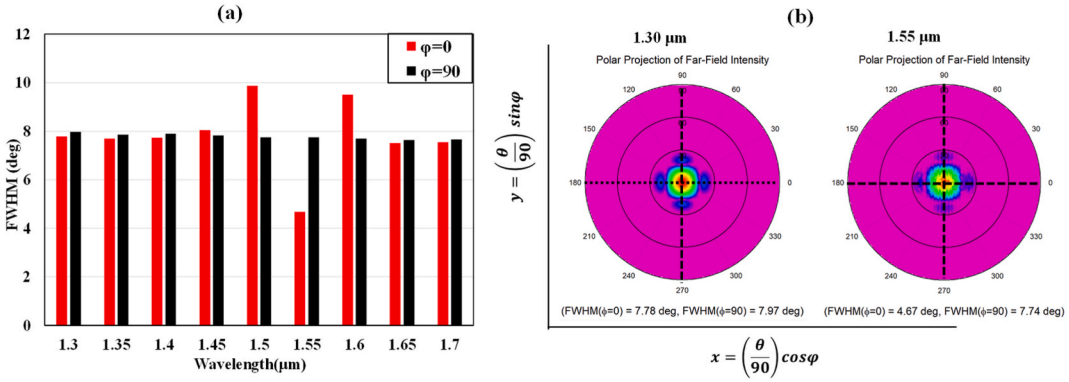

Fig. 11. (a) FWHM as a function of wavelength (FWHM analysis at $\varphi = 0^{\circ}$ evaluate the directional coupler's spectral response for the TE mode, while the FWHM at $\varphi = 90^{\circ}$ assess its spectral response for the TM mode, providing insights into how the coupler behaves under different phase angles). (b) Far-field intensity for demonstrating FWHM. The phase angle of the FWHM depends on the output field in polar coordinates of the far-field transformation.

3.5. Coupling ratio

The coupling ratio (CR) represents the fraction of optical power of the device coupled to the waveguide. The CR for this beam splitter can be calculated using the following equation (7) [35]:

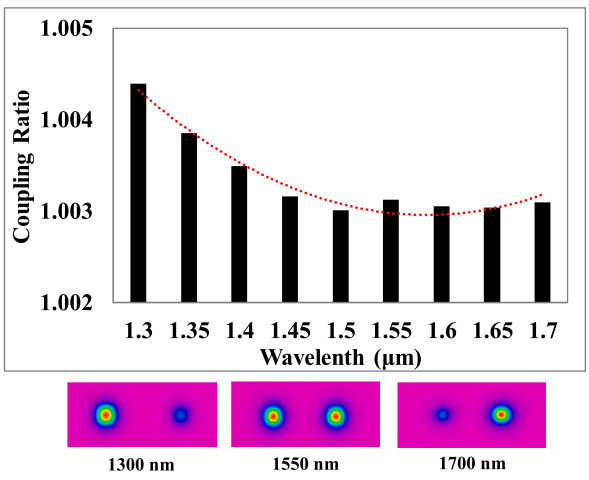

Fig. 12. Coupling ratio as functions of wavelength and NFPs demonstration.

$$CR = \frac{P_{in}}{P_{out\ 1} + P_{out\ 2}} \tag{7}$$

where P_{in} is the input power and $P_{out\ 1}$ and $P_{out\ 2}$ are the powers of the two outputs. The coupling ratio is investigated as a function of the wavelength, and the results are shown in Fig. 12. The output field intensity patterns of the beam splitter at 1300 nm, 1550 nm, and 1700 nm are presented in Fig. 12, which introduces the wavelength-dependent coupling ratio. The beam splitter demonstrates the same splitting ratio (50:50) between the outputs at 1550 nm. At 1300 and 1700 nm, the output light exits at the thru or cross ports, respectively. The coupler functions as a beam splitter, evenly dividing the input light between the thru and cross ports of waveguides with CR > 1.

3.6. Loss analysis

We calculate the excess loss (EL) for this CBS using equation (8) [36] as follows:

$$EL = -10\ log\left(\frac{P_{out\ 1} + P_{out\ 2}}{P_{in}}\right) \tag{8}$$

here $P_{out\ 1}$ and $P_{out\ 2}$ represent the power of the output waveguide at the bar and cross ports, respectively. The excess loss of this SI beam splitter is shown in Fig. 13(a) by varying the wavelength in the range of 1.30–1.70 μm. The loss graph shows that the excess loss gradually decreases with the wavelength, and the excess loss is 0.0135 dB at 1.55 μm. Fig. 13(b) illustrates the relationship between excess loss and polarization manipulation angles at 0–31°. At an angle of 31 °, the coupler exhibits a high degree of polarization-independent profile, with a minimum excess loss of 0.05 dB.

Crosstalk is an important characteristic of an SI beam splitter. We also investigate the crosstalk of this beam splitter by comparing the sum of the desired and undesirable powers of the outputs. We calculate the crosstalk of the beam splitter using equation (9) [37]:

$$\text{Crosstalk} = 10\log_{10}\left(\frac{P_{uw}}{P_{total}}\right) \tag{9}$$

where P_{uw} indicates the magnitude of the undesired intensity and P_{total} is the total intensity of the beam splitter. Fig. 13(c) illustrates the fluctuation of the crosstalk of this coupler across the wavelength range of 1.3–1.7 μm, and the crosstalk of this beam splitter is approximately −25.06 dB. Fig. 13(d) illustrates the crosstalk variation at various polarized angles. At a polarizing angle of 31 °, the coupler exhibits nearly polarization-independent behavior, with a crosstalk value of −19.77 dB.

3.7. Fabrication tolerances

We investigated the deviation between the fabricated beam splitters and designed patterns, comprehensively assessing the impact of the fabricated pattern deviations on the output characteristics of the beam splitter, as shown in Fig. 14. We investigate that the tolerance for the core-width deviation should be 6 ± 0.5 μm, as presented in Fig. 14(a). Similarly, the acceptable variation in the S-bend length can be 5300 ± 200 μm, which reveals a nearly symmetrical distribution of the splitting ratio between the two outputs, with a minor disparity of ±0.05 (a.u.), as illustrated in Fig. 14(b). Furthermore, the tolerance range of the coupling length is 2280 ± 20 μm, as shown in Fig. 14(c). Finally, we determine the separation gap between the two inputs at 29 μm; this gap can have a possible variation of ±0.3 μm, as shown in Fig. 14(d). These detailed analyses can provide the guidelines for fabricating the beam splitters.

4. Conclusion

We have developed high-performance composite SI beam splitters using polymer materials. These SI composite beam splitters exhibit a 50:50 splitting ratio with an output efficiency of 99%. The excess loss of this splitter is 0.014 dB without any polarization impact. When the polarization is applied, the loss reaches 2 dB, which declines to 0.05 dB at the 31-degree incident angle of the input light. Similarly, the crosstalk of this beam splitter is almost −25.06 dB without any polarization, but when we manipulate polarization with the angle of 31°, the crosstalk reaches −19.77 dB from −4.5 dB. Thus, polymer-based SI composite beam splitters could be novel devices for photonic integrated circuits, and the results of this numerical investigation could significantly affect the fabrication of these types of beam splitters.

Data availability statement

Data will be made available on request.

CRediT authorship contribution statement

Noor Afsary: Writing – original draft, Investigation, Formal analysis. **Fariha Tasnim:** Writing – original draft, Investigation, Formal analysis, Conceptualization. **Md Omar Faruk Rasel:** Writing – review & editing, Supervision, Conceptualization. **Takaaki Ishigure:** Writing – review & editing.

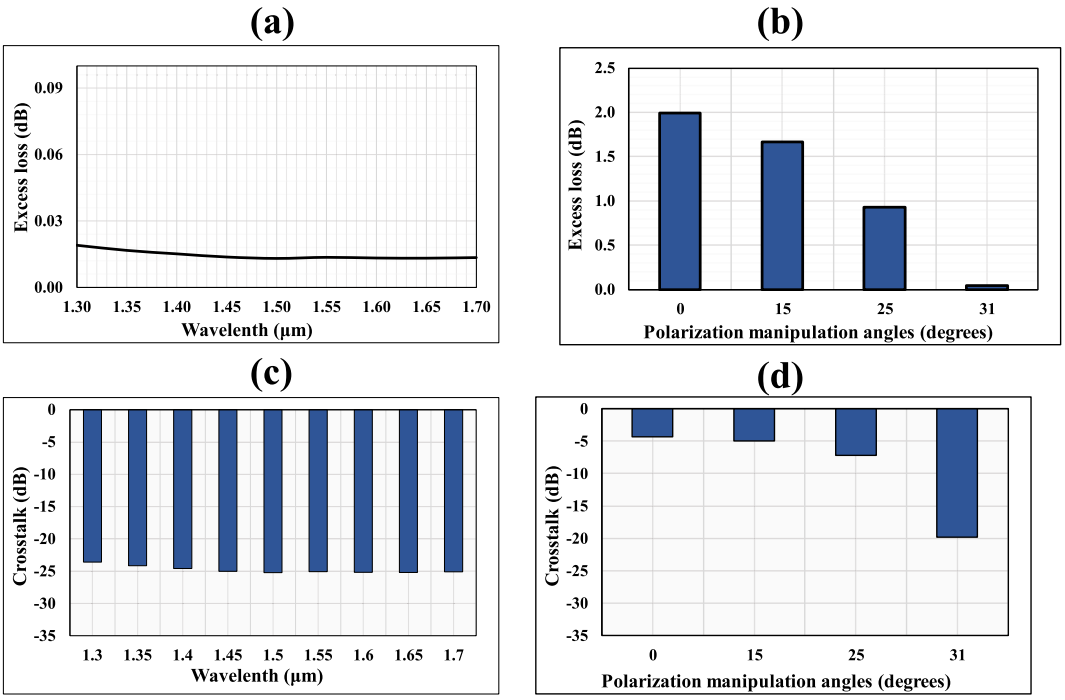

Fig. 13. Excess loss and crosstalk at different wavelengths without manipulation and with polarization manipulation at different angles. (a) Excess loss without any manipulation. (b) Excess loss for manipulated polarized angles. (c) The crosstalk without any manipulation. and (d) Crosstalk with different angles for polarization manipulation.

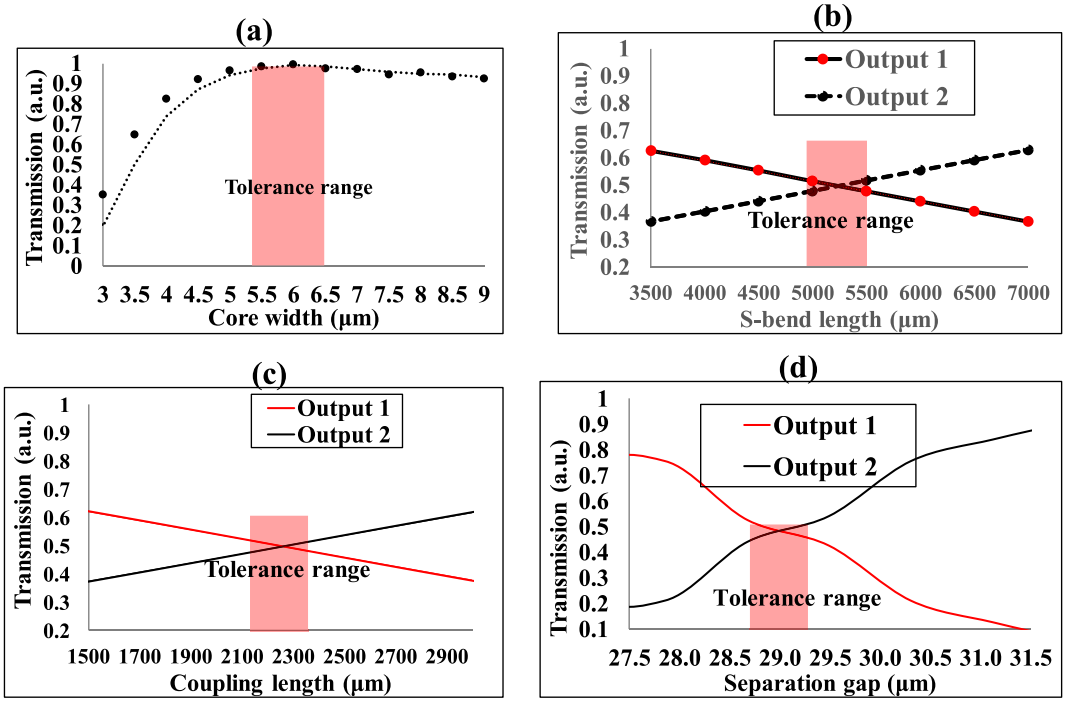

Fig. 14. Fabrication tolerance analysis for the structural parameters of the beam splitter. (a) Tolerance range for the core width as a function of transmission. (b) Tolerance range of the of S-bend length. (c) Tolerance range of the coupling length. (d) Tolerance range for the separation gap between two inputs.

Declaration of competing interest

The authors declare that they have no known competing financial interests or personal relationships that could have appeared to influence the work reported in this paper.

.

References

[1] H. Cho, P. Kapur, K.C. Saraswat, Power comparison between high-speed electrical and optical interconnect for interchip communication, J. Lightwave Technol. 22 (9) (2004) 2021–2033.
[2] D.A.B. Miller, Rationale and challenges for optical interconnects to electronic chips, Proc. IEEE 88 (6) (2000) 728–749.
[3] A. Chu, Y. Lu, Y. Lin, Fabrication and analysis of tantalum pentoxide optical waveguide resonator of high thermal stability, Opt. Express 27 (5) (2019) 6629–6639.
[4] D. Kim, S. Ahn, I. Cho, D. Im, S. Shorab Muslim, H. Park, Fabrication of thermally stable and cost-effective polymeric waveguide for optical printed-circuit board, Opt. Express 16 (21) (2008) 16798–16805.
[5] N. Sherwood-Droz, M. Lipson, Scalable 3d dense integration of photonics on bulk silicon, Opt. Express 19 (18) (2011) 17758–17765.
[6] S. Gross, M. Withford, Ultrafast-laser-inscribed 3d integrated photonics: challenges and emerging applications, Nanophotonics 4 (3) (2015) 332–352.
[7] S.B. Yoo, B. Guan, R.P. Scott, Heterogeneous 2d/3d photonic integrated microsystems, Microsyst. Nanoeng. 2 (2016) 16030.
[8] R. Dangel, F. Horst, D. Jubin, N. Meier, J. Weiss, B. Offrein, B. Swatowski, C. Amb, D. DeShazer, W. Weidner, Development of versatile polymer waveguide flex technology for use in optical interconnects, J. Lightwave Technol. 31 (13) (2013) 3915–3926.
[9] M.O.F. Rasel, N. Afsary, M.K. Alam, F. Tasnim, M.N. Sakib, R. Hatai, T. Ishigure, Step and graded-index core-based polymer multimode interference splitters for photonic integrated circuits, Optik 290 (2023) 171278.
[10] G. Huang, T.H. Park, M.C. Oh, Broadband integrated optic polarization splitters by incorporating polarization mode extracting waveguide, Sci. Rep. 7 (2017) 4789.
[11] J. Ruan, Y. Gao, C. Song, P. Xu, W. Zhang, Y. Chen, X. Shen, Compact reconfigurable on-chip polarization beam splitters enabled by phase change material, Opt. Express 31 (20) (2023) 33091–33102.
[12] R. Zhang, S. Sun, F. Zhang, K. Chen, L. Liu, N. Zhu, Four-mode parallel silicon multimode waveguide crossing scheme based on the asymmetric directional couplers, Opt. Express 30 (13) (2022) 22442–22451.
[13] H. Wu, Ying Tan, Daoxin Dai, Ultra-broadband high-performance polarizing beam splitter on silicon, Opt. Express 25 (6) (2017) 6069–6075.
[14] C. Deng, M. Lu, Y. Sun, L. Huang, D. Wang, G. Hu, R. Zhang, B. Yun, Y. Cui, Broadband and compact polarization beam splitter in LNOI hetero-anisotropic metamaterials, Opt. Express 29 (8) (2021) 11627.
[15] J.S. Penades, A. Ortega-Moñux, M. Nedeljkovic, J.G. Wangüemert-Pérez, R. Halir, A.Z. Khokhar, C. Alonso-Ramos, Z. Qu, I. Molina-Fernández, P. Cheben, G. Z. Mashanovich, Suspended silicon mid-infrared waveguide devices with subwavelength grating metamaterial cladding, Opt. Express 24 (20) (2016) 22908.
[16] X. Xu, L. Ma, Z. He, 3D polymer directional coupler for on-board optical interconnects at 1550 nm, Opt. Express 26 (13) (2018) 16344–16351.
[17] I. Taghavi, R. Dehghannasiri, T. Fan, A. Tofini, H. Moradinejad, A. Efterkhar, S. Shekhar, L. Chrostowski, N. Jaeger, A. Adibi, Enhanced poling and infiltration for highly efficient electro-optic polymer-based Mach-Zehnder modulators, Opt. Express 30 (15) (2022) 27841–27857.
[18] F. Zhang, C. Deng, Y. Huang, X. Zhang, T. Wang, Optimization of the interlayer distance for low-loss and low-crosstalk double-layer polymer optical waveguides, Opt. Express 31 (15) (2023) 23754–23767.
[19] R. Zhang, C. Deng, J. Zhao, F. Zhang, Y. Huang, X. Zhang, T. Wang, Compact and efficient three-mode (de)multiplexer based on horizontal polymer waveguide couplers, Opt. Express 30 (3) (2022) 3632–3644.
[20] G. Woyessa, A. Fasano, A. Stefani, C. Markos, K. Nielsen, H. Rasmussen, O. Bang, Single mode step-index polymer optical fiber for humidity insensitive high temperature fiber Bragg grating sensors, Opt. Express 24 (2) (2016) 1253–1260.
[21] M.K. Alam, N. Afsary, M.O.F. Rasel, T. Ishigure, Multimode interference based Y-branch polymer optical waveguide splitter: design and investigation, Proc. Int. Conf. Electr. Commun. Inform. Technol., ICECIT 2021 (2021), https://doi.org/10.1109/ICECIT54077.2021.9641413.
[22] G. Palma-Vega, D. Hässner, S. Kuhn, J. Nold, F. Möller, C. Jáuregui, A. Tünnermann, N. Haarlammert, T. Schreiber, TMI and polarization static energy transfer in Yb-doped low-NA PM fibers, Opt. Express 31 (15) (2023) 24730–24738.
[23] N. Afsary, M.O.F. Rasel, T. Ishigure, Design and Investigation of Three-Dimensional Polarization-independent Polymer Mach-Zehnder Interferometer at 1550 Nm, Khulna Univ. Stud., Oct. 2022, pp. 83–92.
[24] F. Tasnim, N. Afsary, M. Faruk Rasel, T. Ishigure, Graded-index core-based polarization beam splitters realized with symmetric polymer directional couplers, Opt. Continuum 2 (2023) 1040–1052.
[25] G. Corrielli, S. Atzeni, S. Piacentini, I. Pitsios, A. Crespi, R. Osellame, Symmetric polarization-insensitive directional couplers fabricated by femtosecond laser writing, Opt. Express 26 (12) (2018) 15101–15109.
[26] X. Shi, J. Zhang, W. Fan, Y. Lu, N. Peng, K. Rottwitt, H. Ou, Compact low-birefringence polarization beam splitter using vertical-dual-slot waveguides in silicon carbide integrated platforms, Photon. Res. 10 (1) (2021) A8.
[27] J. Yamauchi, T. Ando, H. Nakano, Beam-propagation analysis of optical fibers by alternating direction implicit method, Electron. Lett. 27 (Aug. 1991) 1663–1665.
[28] Y. Hsueh, M. Yang, H. Chang, Three-dimensional noniterative full-vectorial beam propagation method based on the alternating direction implicit method, J. Lightwave Technol. 17 (11) (1999) 2389–2397.
[29] O. Schwelb, Evolution of the polarization in codirectional and contradirectional optical couplers, J. Opt. Soc. Am. 72 (19) (1982) 1152–1158.
[30] R. Jones, A new calculus for the treatment of optical SystemsI. Description and discussion of the calculus, J. Opt. Soc. Am. 31 (7) (1941) 488–493.
[31] T. Ishigure, Y. Nitta, Polymer optical waveguide with multiple graded-index cores for on-board interconnects fabricated using soft-lithography, Opt. Express 18 (13) (2010) 14191–14201.
[32] K. Abe, Y. Oizumi, T. Ishigure, Low-loss graded-index polymer crossed optical waveguide with high thermal resistance, Opt. Express 26 (4) (2018) 4512–4521.
[33] R.A. Sammut, K. Ghatak, Perturbation Theory of Optical Fibres with Power-Law Core Profile, 1978.
[34] B. Patiño-Jurado, J.F. Botero-Cadavid, J. Garcia-Sucerquia, Analytical study of the numerical aperture of cone-shaped optical fibers: a tool for tailored designs, Heliyon 5 (5) (2019) e01612.
[35] X. Xu, L. Ma, Z. He, 3D polymer directional coupler for on-board optical interconnects at 1550 nm, Opt. Express 26 (13) (2018) 16344–16351.
[36] S. Mao, L. Cheng, C. Zhao, H. Fu, Ultra-broadband and ultra-compact polarization beam splitter based on a tapered subwavelength-grating waveguide and slot waveguide, Opt. Express 29 (18) (2021) 28066–28077.
[37] T. Fujisawa, M. Koshiba, Polarization-independent optical directional coupler based on slot waveguides, Opt. Lett. 31 (1) (2006) 56–58.